Eur. Phys. J. D (2020) 74: 174
https://doi.org/10.1140/epjd/e2020-10120-x

THE EUROPEAN PHYSICAL JOURNAL D

Regular Article

A transportable quantum gravimeter employing delta-kick collimated Bose–Einstein condensates*

Nina Heine[1,a], Jonas Matthias[1], Maral Sahelgozin[1], Waldemar Herr[1], Sven Abend[1], Ludger Timmen[2], Jürgen Müller[2], and Ernst Maria Rasel[1]

[1] Institut für Quantenoptik, Leibniz Universität Hannover, Welfengarten 1, Hannover, Germany
[2] Institut für Erdmessung, Leibniz Universität Hannover, Schneiderberg 50, Hannover, Germany

Received 28 February 2020 / Received in final form 9 June 2020
Published online 25 August 2020

Abstract. Gravimetry with low uncertainty and long-term stability opens up new fields of research in geodesy, especially in hydrology and volcanology. The main limitations in the accuracy of current generation cold atom gravimeters stem from the expansion rate and the residual centre-of-mass motion of their atomic test masses. Our transportable quantum gravimeter QG-1 aims at overcoming these limitations by performing atom interferometry with delta-kick collimated Bose–Einstein condensates generated by an atom chip. With our approach we anticipate to measure the local gravitational acceleration at geodetic campaigns with an uncertainty less than $1\,\mathrm{nm/s^2}$ surpassing the state-of-the-art classic and quantum based systems. In this paper, we discuss the design and performance assessment of QG-1.

1 Introduction

1.1 Terrestrial absolute gravimetry as a research tool in geoscience and applied geophysics

The unique potential of absolute gravimetry lies in measuring and monitoring temporal variations of Earth's gravity field, i.e. mass variations, caused by numerous processes in the hydrosphere, the cryosphere, the atmosphere and in the solid earth on time scales from a few days to multiple years [1–4]. For example, for water management the underground hydrological changes are of interest from local to continental scale. For these large-scale long-term observations of gravity variations, accurate and stable sensors are required. This can only be met by absolute gravimeters, as even the most stable relative meters, the superconducting gravimeters, need to be calibrated not only with respect to their scale but also to know their long-term drift behaviour (temporal change of the measuring zero level), on a regular basis, which sets operational constraints.

Terrestrial absolute gravimetry is a geodetic and geophysical technique to study regional and global tectonics like vertical movements of the continental plate, postglacial isostatic compensation processes, vertical compaction of sediment basins or mountain building [1]. In general, it is applied as a complementary tool to the geometrical methods. By observing gravity variations, the absolute measurements are also very sensitive to height changes and support the definition and control of the height datum. No additional reference or connection points at Earth's surface are needed. The accuracy of an absolute gravity net is independent of geographical extension and the covered gravity range, hence enabling applications on local, regional and global scales with a consistent measurement quality. An independent geometrical verification of vertical displacements is possible by a Global Navigation Satellite System, Very Long Baseline Interferometry or Satellite Laser Ranging.

The monitoring of underground reservoirs within CO_2 capture and storage projects and for geothermal exploitation may become tasks of ground based gravimetry with increasing importance in the future. In geothermal fields in Japan, microgravity monitoring has been successfully established for assessing changes in fluid recharge from reservoir boundaries associated with geothermal water extraction [5,6]. Large variations in gravity associated with production at the Wairakei Geothermal Field in New Zealand have been reported [7]. Baseline surveys were made at 50 to 150 points prior to exploitation, and afterwards at intervals of two to five years. The gravity change in the extraction area is strongly related to the recharged water amount. For monitoring within the Sleipner CO_2 Capture and Storage project in the North Sea [8–10], seismic and gravimetric techniques have been combined allowing an estimation of the amount of dissolved CO_2, which is effectively invisible on solely seismic data. In addition, periodically deployed gravity surveys can serve as an early warning system to detect accumulating CO_2 in shallow overburden traps.

* Contribution to the Topical Issue "Quantum Technologies for Gravitational Physics", edited by Tanja Mehlstäubler, Yanbei Chen, Guglielmo M. Tino and Hsien-Chi Yeh.

[a] e-mail: n.heine@iqo.uni-hannover.de

Quantum gravimeters will improve the economic efficiency of terrestrial gravity campaigns significantly, making it a compulsory tool for various surveys. For example in volcanology, where current observations of active volcanoes are limited by the microseismic background noise [11], quantum gravimeters are potentially less affected due to their integrated vibration management systems. Additionally, the gravity changes recorded on Mount Etna with superconducting gravimeters are in the order of a few ten nm/s^2 [11], highlighting the necessity of a high measurement sensitivity associated with a suitable high temporal resolution. The opportunity for measurements of high accuracy over long time scales [26], provided by quantum gravimeters, will reduce the influence of seasonal variations.

1.2 Determination of local gravity employing atom interferometry

Beginning with proof-of-principle experiments in the 1990s [12–14] inertial sensors based on atom interferometry have undergone a rapid development [15–21]. This technology enabled measurements of local gravity with unprecedented stability [22]. By now, first demonstration setups made their way out of the laboratory into field deployed measurement campaigns [23] as well as campaigns on a ship [24] and in a plane [25]. Recently, even a commercial product became available [26].

The most conventional measurement scheme is a Mach-Zehnder type interferometer based on freely falling atoms interacting with light pulses [27]. A first light pulse puts the atomic wavepacket into an equally populated superposition of motional states, which differ in vertical momentum by the number of photon recoils k_{eff} transferred by the atom light interaction from the laser pulse. After a free evolution time T the two states are separated in height and a second light pulse is applied swapping their momenta. Consequently, the two states are redirected such that they spatially overlap after another time T and are brought to interference by applying a third light pulse, which closes the interferometer. Gravity leads to an additional shift in position of the two trajectories at the second light pulse with respect to its phase fronts, which leads to a difference in imprinted phase between the two trajectories. This phase difference $\Delta\phi$ can be read out by the population difference of the output ports after the atom interferometer sequence and is, to leading order, directly proportional to the local gravitational acceleration g via

$$\Delta\phi = k_{\mathrm{eff}}\, g\, T^2. \tag{1}$$

This measurement principle enables absolute measurements with high stability, as it solely depends on the atomic properties in free fall and their interaction with, in time and frequency, precisely controllable light fields. The technique already demonstrated long-term stability over months [26], while maintaining a measurement rate on the order of 1 Hz. However, over the last years two systematic effects inherent to the atomic source have been identified as limiting the accuracy of present cold atom gravimeters. Their molasses-cooled atomic ensembles cannot be released into free fall with a sufficiently small horizontal centre of mass velocity component, leading to an unknown bias due to the Coriolis force [22,28]. Furthermore, the residual temperature of the atomic ensemble of a few μK in combination with insufficient characterisation of the wavefronts of the interrogation laser beams introduces an unknown bias in the measured acceleration [22,28,29].

A promising route to overcome these limitations is to use colder ensembles released from an optical or magnetic trap [29,30]. Our approach is to use Bose–Einstein condensates (BECs) released from and collimated by a magnetic potential generated with an atom chip [31–34]. Based on a high-flux BEC source [35] and exploiting atom chips, our transportable Quantum Gravimeter (QG-1) will be able to combine the proven benefits of atom interferometry in terms of long-term stability with the beneficial properties of a delta-kick collimated ensemble with a residual expansion energy below 1 nK and the exquisite control over the external degrees of freedom provided by the atom chip technology. Additionally, working with ensembles exhibiting a velocity spread well below one photon recoil, permits the efficient use of Bragg diffraction instead of utilising Raman transitions. This strongly alleviates the demands on radio frequency generation and control, while contributions due to light shifts can be suppressed by the temporal light pulse shape [36,37]. Furthermore, it opens up the domain of multi-order diffraction schemes [21] and spatially resolved detection, giving access to trajectory reconstruction methods for back-correction algorithms. Adding these benefits to the measurement principle will enable to reach measurement uncertainties in the sub nm/s^2 regime.

2 Setup

The transportable Quantum Gravimeter consists of two main parts: the sensor head (Fig. 1), in which the gravity measurement is performed, and a driving unit, where the laser system, the control electronics, and the computer system are placed in a temperature stabilised transportable rack.

2.1 Sensor head

The demonstration of the high-flux BEC source [35] suggested the application of BECs for high precision measurements in compact sensors. The adaption of the source concept for a dedicated gravimeter setup is detailed in the following.

The overall setup is supported by three aluminium profiles placed on adjustable feet and can coarsely be divided into four parts: (i) the ultracold atom source, (ii) the atom interferometry section, (iii) the magnetic shield, and (iv) the vibration management system.

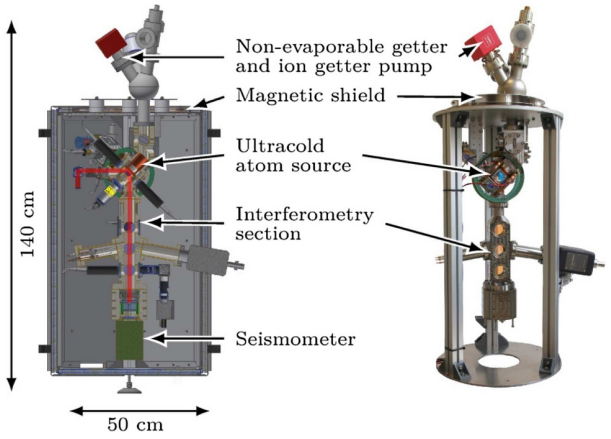

Fig. 1. Photograph and conceptual design section view of the sensor head of the QG-1 setup. The photograph depicts the system before mounting of the collimation and detection optics, as well as the magnetic shield. In the section view the interferometry laser beam path is highlighted.

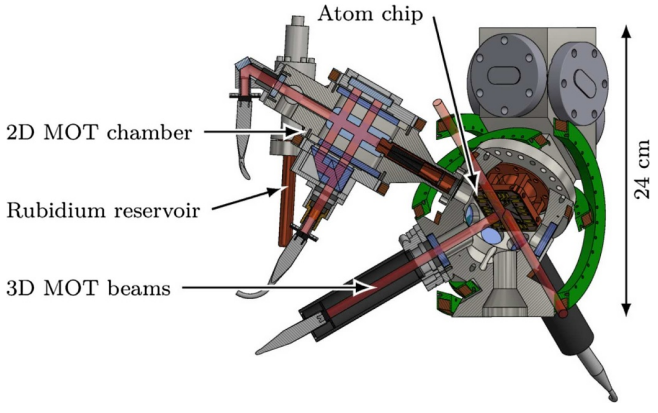

Fig. 2. Conceptual design section view of the double MOT setup with indicated cooling laser beams. The double MOT setup consists of the 2D MOT chamber for pre-cooling the rubidium atoms leaving the reservoir. A beam of pre-cooled atoms is guided through a differential pumping stage into the main experimental chamber. In the main chamber the atoms are confined and further cooled in a 3D mirror MOT. The trapping fields are produced by the atom chip and homogeneous offset field coils.

2.1.1 Ultracold atom source

The high-flux BEC source is set up in a double magneto-optical trap (MOT) configuration (Fig. 2). Vaporised ^{87}Rb is loaded into a source chamber, where a 2D$^+$ MOT [38,39] pre-cooles and confines the atoms into a beam, which is injected into the main chamber via a differential pumping stage. In the main chamber the atoms are captured in a three dimensional (3D) atom chip MOT in mirror geometry [32].

The atom chip assembly consists of three current carrying layers (Fig. 3) creating magnetic fields required for different phases of the experiment [32]. The upmost layer is covered by a 2 μm thick dielectric mirror coating optimised for 780 nm light with an angle of incidence of 45°.

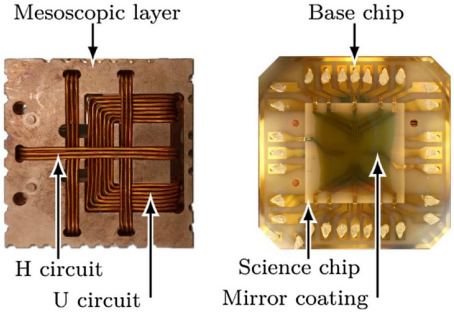

Fig. 3. Photograph of the atom chip assembly. The mesoscopic layer produces magnetic fields for the MOT configuration and the transfer to the Ioffe–Pritchard-type trap provided by the chips. The Base and Science chip provide the magnetic fields for transfer and the final trap geometry for efficient evaporation. The mirror coating is used for the MOT configuration and redirects the interferometry beam.

Beside its use for the 3D mirror MOT configuration it redirects the interferometer light field to be collinear to gravity (Fig. 4). This configuration has been chosen to guarantee an unobstructed beam path, avoiding diffraction of the interferometer beam at the chip edge.

The lowest of the three chip layers, the mesoscopic layer, is a set of insulated copper wires placed in inlets of a copper mount. The wires form a U- and an H-shaped structure [33]. The U-shaped circuit consists of seven windings. In combination with a homogeneous offset field it produces the magnetic quadrupole field for the 3D atom chip MOT [33]. To increase the transfer efficiency of the molasses-cooled atoms into a magnetic trap with tight confinement for fast evaporation, a combination of circuits is used. The atoms are loaded into a shallow magnetic trap with a geometrical mean trapping frequency of approximately 30 Hz, which is produced by the H structure of the mesoscopic layer and a Z structure on the second layer, the base chip [35]. The tight Ioffe–Pritchard type trap [40,41] for fast evaporation with a geometrical mean trapping frequency around 250 Hz is formed by the base chip in combination with the third layer, the science chip. In this trap configuration the phase space density of the ensemble is increased until surpassing the critical point for condensation by forced evaporation before the atoms are released into free fall. During free fall the expansion rate of the BEC is controlled by a magnetic lensing procedure and the atoms are transferred into the $|5S_{1/2}\ F = 2, m_F = 0\rangle$ Zeeman sublevel via an adiabatic rapid passage.

2.1.2 Atom interferometry section

After external and internal state preparation the freely falling atoms enter the atom interferometry section. This section features three zones for optical access to further manipulate or detect the atomic ensemble. The distance between the atom chip and the most distant detection zone is 321 mm (Fig. 4), allowing for a total free fall time of 256 ms. During free fall the atoms are manipulated by the light fields as described in Section 1.2. These

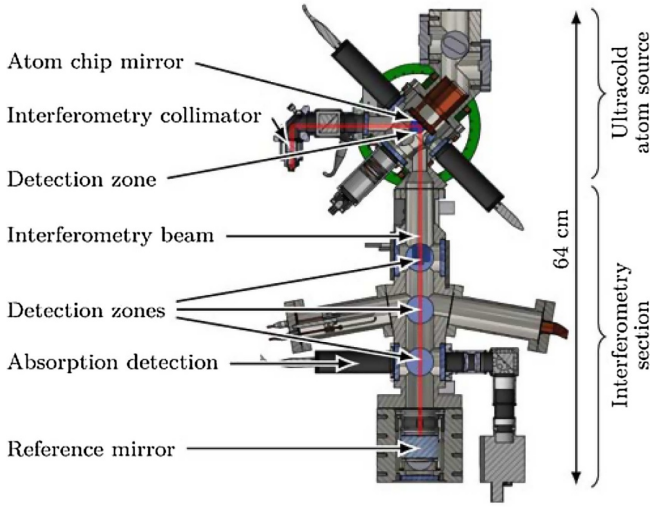

Fig. 4. Conceptual design section view of the high-flux source and the interferometry section. The collimated and polarisation purified laser beam enters the experiment chamber through a vacuum window, is reflected at the atom chip mirror and retro-reflected by a tilt-able mirror of high optical quality. The atomic sample can be detected by absorption imaging at four detection zones.

pulses are sent from the laser system to the sensor head via a polarisation maintaining fibre and collimated to a free-space beam with a diameter of 5.2 mm. After passing a polarising beam splitter and a quarter waveplate the light field is circularly polarised, enters the vacuum chamber horizontally via an angled wedged vacuum view port, and is reflected by the chip mirror to propagate vertically towards the free-falling atoms. The beam is retro-reflected from an in-vacuum mirror mounted on a tip-tilt stage to generate the counter-propagating beam for the coherent manipulation of the atoms. The retro-reflection mirror is an etalon substrate of 30 mm thickness and 50.8 mm diameter with a surface flatness better than $\lambda/20$ at 633 nm over the diameter of the substrate and is covered by a highly reflective dielectric coating for 780 nm. The substrate's backside features an anti-reflection coating at 780 nm to allow for adjustment of the sensor head orientation using the residual light. The mirror is placed in a titanium holder actuatable by three piezo stacks, which allow a maximum tilt of 2 mrad for the mirror. To compensate for Earth's rotation rate a tilt of 0.019 mrad is required for 256 ms of free fall time. With this arrangement, atom interferometers of different duration, and thereby different sensitivity, can be formed and detected in the three zones along the dropping tube. For example, for an interferometer with a contrast of 90 %, an atom number of 10^5, a momentum transfer of $2\,\hbar k$ (here $\hbar$ is the reduced Planck constant and k is the wave vector) and a pulse separation time of 100 ms a single shot sensitivity of $2 \times 10^{-8}\,\mathrm{m/s^2}$ is reached while providing a cycle rate of 0.5 Hz. The detection is done via absorption imaging using a spatially resolving charge-coupled device (CCD) camera, which delivers information about the atom number, density and position of the BEC at the same time. At the upmost and lowest detection zone four view ports are mounted, allowing for two perpendicular detection systems to obtain the full three dimensional information of the position and shape of the BEC. After the closing interferometer pulse the output states are left to separate spatially and can be detected in the same image simultaneously. With this method information about the evolution of all states involved can be obtained in one single detection process.

2.1.3 Magnetic shielding

The shield is designed as a hexagonal tube made from Mu-metal mechanically enforced by wooden and aluminium layers between the Mu-metal sheets. The Mu-metal layers provide shielding against low frequency disturbances up to tens of Hz, while the aluminium layer reduces radio frequency components [42,43]. To provide lowest residual magnetic fields and field gradients inside the shielded volume an equilibration procedure is required. A similar design has demonstrated a residual magnetic field gradient of 2.5 nT/m [44].

2.1.4 Vibration management

The instrument's high sensitivity to accelerations makes it prone to vibrational disturbances inevitably occurring at measurement locations. Precautions are taken to decouple QG-1 form these environmental vibrations. Concepts for correlation of the atom interferometric measurements with mechanical or opto-mechanical sensors [45,46], represented by the seismometer in Figure 1, are foreseen. Additionally, the compact design of the apparatus allows it to be placed on a passive vibration isolation platform with a maximum load capacity of 123 kg.

2.2 Driving unit

The laser system and driving electronics are placed inside a temperature stabilised rack of 1.4 m height on heavy duty wheels. Experiment control is done by field programmable gate array based compact electronic modules and a miniature computer for programming the sequence and collecting, storing, and evaluating the data, providing autonomous operation of the instrument. The compact electronic modules, originally developed for space applications [47], are used to generate the atom chip and offset field coil currents, as well as the radio frequencies and control currents for the laser system.

The laser light generation and amplification relies on telecom based fibre coupled components to grant long-term maintenance-free operation [48] (Fig. 5). A fibre coupled narrow linewidth external cavity diode laser (ECDL) emitting at 1560 nm is used as a master laser, which is stabilised to the $|F = 3\rangle$ to $|F' = 4\rangle$ transition of the ^{85}Rb D2-line. For this purpose the laser is frequency doubled by a periodically poled lithium niobate wave guide mixer before entering a modulation transfer spectroscopy

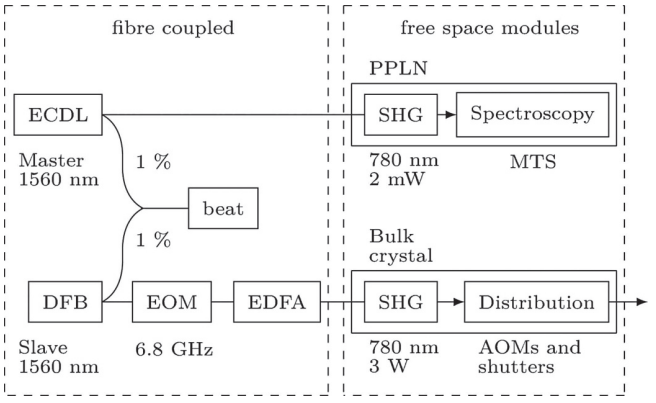

Fig. 5. Concept of the laser system for atom cooling and interferometry. Left: fibre coupled components operating at a wavelength of 1560 nm including the master external cavity diode laser (ECDL) and slave distributed feedback (DFB) diode laser. The slave laser is frequency stabilised to the master laser using the beat note. The slave laser frequency is modulated by an electro-optic modulator (EOM), adding a frequency side band to drive repumping transitions. The modulated light is then amplified by an erbium-doped fibre amplifier (EDFA). Right: The frequency of the driving lasers is doubled to the Rb D_2 lines in two separate free space modules. The master laser is used for a modulation transfer spectroscopy (MTS) setup, while the slave laser is distributed to individually controllable paths for cooling in the 2D and 3D MOT and Bragg interferometry. The light is then guided to the sensor head by polarisation maintaining fibres.

(MTS) setup [49] in a free space module. To provide a versatile laser frequency control a fibre coupled distributed feedback (DFB) diode laser with a current controllable modehop-free tuning range of 12.8 GHz at 1560 nm is offset locked to the stabilised master ECDL. To generate the frequency to drive the ^{87}Rb $|F = 1\rangle$ to $|F' = 2\rangle$ repumping transition, the light from the DFB diode is phase modulated at 6.8 GHz with a fibre electro-optical modulator (EOM). The modulated light is amplified to an output power of up to 15 W by an erbium-doped fibre amplifier (EDFA) before it is guided to a free space single pass frequency doubling stage. Here, a second harmonic generation (SHG) process provides up to 3 W of light power at 780 nm. The beam is then divided into individual paths for operating the 2D$^+$ and 3D MOT, fluorescence and absorption detection and Bragg interferometery, each controllable by an acousto-optic modulator (AOM) and mechanical shutters. In the interferometry path two frequency components separated by the Doppler frequency plus two times the photon recoil frequency are required to drive Bragg transitions. Depending on the free fall time the Doppler shift causes this frequency difference to span from a couple of kHz to 6.4 MHz for the maximum free fall time in our setup. Due to the modest frequency difference both frequency components can be generated in one single AOM [21]. Both light fields are coupled into the same polarisation maintaining fibre and all laser beams are guided to the sensor head using polarisation maintaining optical fibres.

3 Performance estimation

This section summarises the performance estimation with respect to the accuracy for QG-1, focusing on the motion-induced uncertainty contributions, since these constitute the leading order uncertainties in present atomic gravimetry. Additionally, two effects related to the ultracold atom source are investigated. The first is induced by blackbody radiation [50,51], especially during the vicinity of the atoms to the warmed-up atom chip, and the second by the interactions of the atoms within the BEC.

3.1 Motion-induced uncertainty contributions

To perform an accurate determination of local gravity the knowledge of the starting conditions of the measurement is crucial. The properties of interest are the ensembles' initial position, velocity, and velocity distribution, which are directly related to phase contributions due to wave front aberrations and coupling to rotations [22,28]. In atom gravimeters operated with laser cooled atoms the ensemble is released into free fall from a molasses stage. Therefore, the starting conditions highly depend on the intensity balance and polarisation quality of the light fields irradiating the atoms from six directions. From the uncertainty of 4 nm/s^2 stated in reference [28] an uncertainty in horizontal velocity of 55 μm/s can be inferred for the cold atom gravimeter. The minimal ensemble temperature of cold atom gravimeters is restricted to temperatures of few μK by the recoil limit. Filtering with Raman selection can reduce the effective horizontal temperature in the according dimensions, but is also strongly reducing the number of interrogated atoms.

In contrast to cold atom gravimeters, the atom chip technology of QG-1 in combination with the absorption detection systems is estimated to resolve the centre of mass positions of the wavepackets better than one micrometer at the two detection zones separated by 256 ms of free fall time, by this the horizontal velocity better than 4 μm/s, and enables expansion rates equivalent to less than 1 nK [31].

3.1.1 Wavefront aberrations

In state-of-the-art cold atom gravimeters the dominant uncertainty contribution stems from aberrations on the wavefronts of the interferometer light field in combination with the ballistic expansion of the atomic ensemble probed within the atom interferometer [22,28,52,53]. In a simplified picture, assuming a parabolic curvature of the wavefront, the shift of the interferometer phase due to this aberration can be described via

$$\Delta\Phi_{\mathrm{WF}} = \frac{k_{\mathrm{eff}}}{R}\frac{k_{\mathrm{B}}T_{\mathrm{at}}}{m}T^2, \tag{2}$$

where R is the wavefront radius of curvature, T_{at} is the ensemble temperature, m is the mass of a rubidium atom and k_{B} is Boltzmann's constant [28]. In this framework,

for $R = 1\,\mathrm{km}$ and $T_{\mathrm{at}} = 1\,\mathrm{nK}$, the expected bias $\Delta\Phi_{\mathrm{WF}}$ of $15\,\mu\mathrm{rad}$ corresponds to a bias in acceleration of $0.1\,\mathrm{nm/s^2}$. Refining this framework by taking into account a gaussian beam with a waist diameter of 5.2 mm at a distance of 12.5 m from the collimation lens and the optical elements it passes to evaluate the wavefront curvature for each of the light pulses [54,55], the total interferometer phase shift is calculated to be $110\,\mu\mathrm{rad}$, leading to a bias of $0.69\,\mathrm{nm/s^2}$ on the gravity value. Assuming to be able to place the collimation lens within $\pm 10\,\mu\mathrm{m}$ of the required distance, which corresponds to a change of $\pm 0.75\,\mathrm{mm}$ in the beam diameter at 12.5 m distance, the maximum uncertainty of the bias amounts to $0.4\,\mathrm{nm/s^2}$. However, higher order effects need to be taken into account to describe the full experimental reality. In reference [29], exercising a more sophisticated model for the wavefronts and comparing the results with measurements performed on atomic ensembles of different temperatures ranging from $7\,\mu\mathrm{K}$ down to 50 nK, it has been shown, that the associated uncertainty contribution has been reduced from $40\,\mathrm{nm/s^2}$ to $13\,\mathrm{nm/s^2}$. In QG-1 we will continue this work to temperatures below 1 nK and probe different positions within the interferometry beam utilising our compact ensembles to characterise higher order effects.

3.1.2 Coriolis force

If the probed atomic ensemble has a non-zero horizontal centre of mass velocity, the two trajectories of the interferometer arms open up a horizontal area. Thereby, the measured phase difference becomes dependent on the rotation rate of the interferometer around the normal axis of this area by

$$\Delta\phi_{\Omega_{\mathrm{E}}} = 2\,\boldsymbol{\Omega_{\mathrm{E}}}\,(\boldsymbol{k_{\mathrm{eff}}} \times \boldsymbol{v_{\mathrm{at}}})\,T^2, \tag{3}$$

where $\boldsymbol{\Omega_{\mathrm{E}}}$ is the rotation rate and $\boldsymbol{v_{\mathrm{at}}}$ is the velocity of the atoms. This is known as Sagnac effect and leads to the second most significant uncertainty contribution in the determination of the gravitational acceleration in cold atom gravimeters [22,28].

For QG-1 the absorption detection system at the release zone enables the observation of the initial centre of mass position of the atomic ensemble for up to 20 ms time-of-flight. After the interferometer sequence and a total time-of-flight of up to 256 ms, the two output ports will as well be detected via absorption imaging, allowing for a resolution in horizontal centre of mass velocity below $4\,\mu\mathrm{m/s}$ per cycle. This reduces the uncertainty due to the Coriolis force to less than $0.3\,\mathrm{nm/s^2}$ for QG-1.

3.2 Blackbody radiation induced uncertainty contribution

The electric polarisability of the atoms leads to an additional force F_{BBR} given by the gradient of an electric background field potential ∇V_{BBR} [56]. In an environment out of energetic equilibrium a non-homogeneous background radiation field at the position of the atoms will form. The integrated spectral radiance at the position of the atoms can be approximated by estimating the radiating surfaces to have the properties of a blackbody at temperature T to be

$$L(T)\cos(\beta)\,\mathrm{d}A\,\mathrm{d}\Omega = \frac{\pi\,k_{\mathrm{B}}^4}{60\,\hbar^3\,c^2}T^4\cos(\beta)\,\mathrm{d}A\,\mathrm{d}\Omega, \tag{4}$$

where $\cos(\beta)\,\mathrm{d}A$ is the emitting area projected to the direction β of radiation and $\mathrm{d}\Omega$ is the solid angle element into which the radiation is emitted. k_{B} is the Boltzmann constant, $\hbar$ is the reduced Planck's constant and c is the speed of light in vacuum. Taking the radiating surfaces to be of a Lambertian type, the flux density E_e can be computed using ray tracing via

$$E_e = \int_{d\Omega} L(T)\cos(\beta)\,\mathrm{d}A\,\mathrm{d}\Omega. \tag{5}$$

The potential seen by the atoms by the blackbody radiation is then

$$V_{\mathrm{BBR}} = -\frac{1}{2}\,\alpha_{\mathrm{Rb}}\,\frac{E_e}{\epsilon_0\,c}, \tag{6}$$

where α_{Rb} is the ^{87}Rb D2 static scalar polarisability and ϵ_0 is the vacuum permittivity. To assess the influence on the gravity value the induced bias acceleration $a_{\mathrm{BBR}} = F_{\mathrm{BBR}}/m$, where m is the mass of the atom, is calculated.

For QG-1, the presence of the warmed-up atom chip surface on one side of the atoms introduces a temperature gradient resulting in an attractive force for the atomic ensemble. To estimate this effect, a ray tracing simulation of the freely falling atoms was performed to compute the spatial dependence of a_{BBR}. This simulation attributes a bias acceleration due to the blackbody radiation field of $1\,\mathrm{nm/s^2}$. Monitoring the temperature distribution within QG-1 with standard temperature sensors showing an uncertainty of 0.3 K will lead to an estimated uncertainty of $0.3\,\mathrm{nm/s^2}$.

3.3 Mean field interactions induced uncertainty contribution

An important driver for BEC dynamics are the interactions between the atoms within the ensemble of high phase space density. When using BECs for interferometry the arising shift in energy due to these collisions needs to be accounted for. As long as the first beam splitter of the interferometer is symmetric, the atomic densities along the two trajectories can be seen as identical and no net differential phase shift will be acquired during the interferometer by this effect [57]. However, when the first beam splitter shows an asymmetry, the phase evolution along one arm differs from the second driven by the difference in the ensemble's densities. In a mean-field approach, the energy per particle due to interactions of the atoms is given by

$$\frac{E_{\mathrm{int}}(t)}{N} = \frac{g_{\mathrm{int}}}{2}\left\langle |\psi(x,t)|^2 \right\rangle, \text{ with } \int_{\boldsymbol{R}^3} n(x,t)\,\mathrm{d}^3x = N, \tag{7}$$

Table 1. Estimated leading order uncertainty contributions for the QG-1 apparatus.

Systematic effect	Estimated uncertainty (nm/s^2)
Wavefront abberations induced	0.4
Coriolis force induced	0.3
Blackbody radiation induced	0.3
Meanfield interactions induced	0.2
Total	0.8

N being the particle number of the BEC, $g_{\mathrm{int}} = 4\,\pi\,\hbar^2\,a/m$ the interaction parameter, a the scattering length and m the mass of an atom [58].

In the QG-1 setup the atomic ensemble with $N = 10^5$ atoms will have a longitudinal and radial Thomas-Fermi radius of $70\,\mu$m and $120\,\mu$m, respectively, 20 ms after release, when the magnetic lens is applied. This ensemble features an energy per particle per $\hbar$ of 0.75 rad/s. Given the duration of the interferometer of $2T = 200$ ms, an average instability of the first beam splitter ratio of 10^{-4} will lead to an uncertainty in the determination of gravity of $0.2\,\mathrm{nm/s^2}$.

4 Conclusion

We have presented a concept for a transportable BEC gravimeter, outlining possibilities to overcome current limitations to the accuracy of atom gravimeters by adopting alternative atom source concepts. This results in a prospected uncertainty smaller than $1\,\mathrm{nm/s^2}$ as summarised in Table 1.

Furthermore, the atom chip technology grants a vast spectrum of manipulation processes to investigate these systematic effects and verify the given uncertainty estimations. The temperature of the atoms can be set by the evaporation duration. The expansion rate of the ensemble can be adjusted by the magnetic lens and the release procedure. The starting position and velocity are tunable by the magnetic fields for the trap geometry. This gives the opportunity to obtain a unique understanding on how the single atomic properties affect the gravity measurement and build up a comprehensive uncertainty budget.

By making these techniques available for the geoscientific community a valuable contribution to the study of hydrological processes can be made [2], as quasi continuous observations instead of episodic ones reduce the influence of seasonal variations on the signal [59]. Quantum gravimeters, especially when employed in networks, will support the understanding and modelling of our dynamic earth [2].

Open access funding provided by Projekt DEAL. We acknowledge financial support by the Deutsche Forschungsgemeinschaft (DFG, German reaserch foundation) in the project A01 of the SFB 1128 geo-Q and under Germany's Excellence Strategy – EXC 2123 QuantumFrontiers – 390837967 and from "Niedersächsisches Vorab" through "Förderung von Wissenschaft und Technik in Forschung und Lehre" for the initial funding of research in the new DLR-SI Institute. We thank the QUANTUS and MAIUS team and Dr. Amado Bautista-Salvador and Dr. Martina Wahnschaffe from the group of Prof. Dr. Christian Ospelkaus for the collaboration in the atom chip production process. N.H. and W.H. thank Dr. C. Schubert for helpful discussions. S.A. thanks the German Space Agency (DLR) for support with funds by the Federal Ministry of Economic Affairs and Energy (BMWi) under grant No. DLR 50RK1957 (QGYRO).

Author contribution statement

E.M.R. and J. Mü initiated and supervised the project. J. Mü and L.T. assessed the geodetic demands on the instrument and the resulting design criteria. J. Ma., M.S., N.H., S.A., W.H. and E.M. R. designed the instrument. J. Ma., M.S. and N.H. built the instrument. N.H. and W.H. prepared the physics viewpoint and L.T. contributed the geodetic viewpoint to the manuscript. All authors critically reviewed and approved the final manuscript.

References

1. L. Timmen, in *Sciences of Geodesy-I*, edited by G. Xu (Springer, Berlin Heidelberg, 2010)
2. M. Van Camp et al., Rev. Geophys. **55**, 4 (2017)
3. A. Lambert et al., J. Geodyn. **41**, 1 (2006)
4. D. Crossley et al., Rep. Prog. Phys. **76**, 4 (2013)
5. M. Sugihara, T. Ishido, J. Geophys. **73**, 6 (2008)
6. J. Nishijima et al., IOP Conf. Ser. Earth Environ. Sci. **42**, 1 (2016)
7. T.M. Hunt, in *Encyclopedia of Sustainability Science and Technology*, edited by R. Meyers (Springer, New York, 2017)
8. A. Chadwick et al., *Best Practice for the Storage of CO_2 in Saline Aquifers – Observations and Guidelines from the SACS and CO2STORE Projects* (British Geological Survey, Nottingham, 2008)
9. H. Alnes et al., Energy Proc. **4**, 5504 (2011)
10. A.K. Furre et al., Energy Proc. **114**, 3916 (2017)
11. D. Carbone et al., Earth Sci. Rev. **169**, 146 (2017)
12. M.A. Kasevich, S. Chu, Appl. Phys. B **54**, 321 (1992)
13. A. Peters et al., Metrologia **38**, 1 (2001)
14. A. Peters et al., Nature **400**, 6747 (1999)
15. A. Gauguet et al., Phys. Rev. A **78**, 4 (2008)
16. J.K. Stockton et al., Phys. Rev. Lett. **107**, 13 (2011)
17. Z.K. Hu et al., Phys. Rev. A **88**, 4 (2013)
18. P. Berg et al., Phys. Rev. Lett. **114**, 6 (2015)
19. M. Hauth et al., Appl. Phys. B **113**, 1 (2013)
20. A. Bertoldi et al., Eur. Phys. J. D **40**, 2 (2006)
21. S. Abend et al., Phys. Rev. Lett. **117**, 20 (2016)

22. C. Freier et al., J. Phys.: Conf. Ser. **723**, 012050 (2016)
23. X. Wu et al., Sci. Adv. **5**, 9 (2019)
24. Y. Bidel et al., Nat. Commun. **9**, 9 (2018)
25. Y. Bidel et al., J. Geodesy **94**, 9 (2020)
26. V. Ménoret et al., Sci. Rep. **8**, 1 (2018)
27. M.A. Kasevich, S. Chu, Phys. Rev. Lett. **67**, 2 (1991)
28. A. Louchet-Chauvet et al., New J. Phys. **13**, 6 (2011)
29. R. Karcher et al., New J. Phys. **20**, 11 (2018)
30. J.E. Debs et al., Phys. Rev. A **84**, 3 (2011)
31. H. Müntinga et al., Phys. Rev. Lett. **110**, 9 (2013)
32. J. Reichel et al., Phys. Rev. Lett. **83**, 17 (1999)
33. S. Wildermuth et al., Phys. Rev. A **69**, 3 (2004)
34. P. Hommelhoff et al., New J. Phys. **7**, 3 (2015)
35. J. Rudolph et al., New J. Phys. **17**, 6 (2015)
36. E. Giese et al., Phys. Rev. A **94**, 6 (2016)
37. S. Hartmann et al., Phys. Rev. A **101**, 053610 (2020)
38. S. Chandhuri et al., Phys. Rev. A **74**, 2 (2006)
39. K. Diekmann et al., Phys. Rev. A **58**, 3891 (1998)
40. D.E. Pritchard, Phys. Rev. Lett. **51**, 15 (1983)
41. Y.T. Baiborodov et al., J. Nucl. Energy Part C Plasma Phys. **5**, 409 (1963)
42. I. Altarev et al., J. Appl. Phys. **117**, 23 (2015)
43. I. Altarev et al., Rev. Sci. Instrum. **85**, 7 (2014)
44. E. Wodey et al., Rev. Sci. Instrum. **91**, 035117 (2020)
45. L.L. Richardson et al., arXiv:1902.02867 (2019)
46. J. Le Gouët et al., Appl. Phys. B **92**, 133 (2008)
47. D. Becker, M.D. Lachmann, S.T. Seidel et al., Nature **562**, 391 (2018)
48. F. Theron et al., Appl. Phys. B **118**, 1 (2015)
49. J.J. Snyder et al., Opt. Lett. **5**, 4 (1980)
50. M. Sonnleitner et al., Phys. Rev. Lett. **111**, 2 (2013)
51. P. Haslinger et al., Nat. Phys. **14**, 3 (2018)
52. V. Schkolnik et al., Appl. Phys. B **120**, 311 (2015)
53. A. Wicht et al., Phys. Rev. A **72**, 2 (2005)
54. G. Wilpers et al., Appl. Phys. B **76**, 149 (2003)
55. C. Schubert et al., arXiv:1312.5963 (2013)
56. S. Micalizio et al., Phys. Rev. A **69**, 5 (2004)
57. R. Jannin et al., Phys. Rev. A **92**, 1 (2015)
58. M. Meister et al., *Advances in Atomic, Molecular, and Optical Physics* (Academic Press, 2017)
59. M. Van Camp et al., J. Geophys. Res. Solid Earth **110**, B5 (2005)